CIRP Annals - Manufacturing Technology 72 (2023) 193–196

Contents lists available at ScienceDirect

CIRP Annals - Manufacturing Technology

journal homepage: https://www.editorialmanager.com/CIRP/default.aspx

Surface topography and melt pool behavior in rapid turnaround regions of laser powder bed fusion additive manufacturing of nickel superalloy 625

Jason C. Fox (3)[a,*], Chris J. Evans (1)[a,b], Jordan S. Weaver[a], Jesse K. Redford[a,b]

[a] *National Institute of Standards and Technology, 100 Bureau Drive, Gaithersburg, MD, 20899, United States*
[b] *Center for Precision Metrology, University of North Carolina at Charlotte, 9201 University City Blvd., Charlotte, NC, 28223, United States*

A R T I C L E I N F O

Article history:
Available online 17 April 2023

Keywords:
Additive manufacturing
Surface analysis
Nickel alloy

A B S T R A C T

The complexity and vast number of influencing variables in laser powder bed fusion have hindered the development of correlations between surface topography and part performance or process variables. To address this, we investigated the melt pool behavior in regions of the part where a rapid back-and-forth scan strategy occurs. Analysis of surface topography and melt pool cross section geometry on nickel superalloy 625 samples helped identify their relationship. From this, a conceptual model was developed and the implication this has for the development of strong, process-informed correlations is discussed.

Published by Elsevier Ltd on behalf of CIRP.

1. Introduction

Additive manufacturing (AM) has opened a wide range of capabilities, which allow for highly-customized parts with shorter lead times and less material waste [1]. Of the various AM technologies, laser powder bed fusion (LPBF) has developed great interest due to its versatility with a wide range of materials [2]. However, the vast number of variables in the process makes qualification non-trivial compared to more widely used manufacturing methods. Researchers are addressing the qualification at many points in the process. This includes in-process via in-situ monitoring systems [3,4] and post process via destructive and non-destructive evaluation (NDE) and testing (NDT) [5], though additional research and standards are still needed for greater adoption of AM technologies [6].

In other industries, surface topography has been used successfully as a process signature in qualification for several decades [7,8]. To achieve this end for LPBF, a strong understanding of the relationship between process parameters, surface topography, and part performance is required [9]. While there have been significant contributions to our understanding of melt pool geometries, microstructure, and part performance [10–12], our understanding of surface topography is not yet at the level required to use it as a process signature.

To address this, Yadroitsev et al. provided highly detailed analysis of the formation of single tracks [13] and extended this to the effect of hatch spacing (i.e., distance between laser scan tracks) of multi-track pads [14] on melt pool cross section geometry and surface topography. Conceptual models to understand the melt and solidification in regions with denudation, balling, distortion, and irregularities as well as changes in track height, melt pool cross section width, and remelted depth were presented.

Toward a similar goal, Fox et al. used high speed in-situ monitoring systems to gather evidence for the physical mechanisms that create the surface topography [15]. The work provided evidence for "frozen" snapshots of the melt pool geometry at the end of single track experiments. Reese et al. expanded upon this finding, suggesting a relationship between melt pool length and chevron patterns found on the surfaces of single-track experiments [16].

Prior work by the authors also investigated stripe boundaries (i.e., where laser tracks start and/or end within a part based on the scan strategy) [17]. In that work, all stripe boundaries were shown to have double-wide melt pools (i.e., where the width of the melt pool spans two laser scan tracks) and a conceptual model was presented to describe the thermal conditions that led to these formations [17]. Additionally, larger distortions of the melt pool were attributed to rapid turnaround regions (RTRs). RTRs occur when the stripe boundaries intersect with the edge of the part, creating shortened laser track lengths and increasing residual heat [18]. This has consistently created a buildup of material with height variations greater than the 40 µm layer height [17].

To better understand the surface topography in these RTRs, surface and melt pool cross-section measurements of samples built in nickel superalloy (aka., Inconel) 625 (IN625) were compared. Stripe boundaries can create RTRs, but RTRs can also occur solely as a function of part geometry and/or laser scan strategy. This detail was used to develop an RTR design for minimal variability amongst samples. From the results presented, a conceptual model for understanding the melt pool behavior in these RTRs is described, and the potential implications of the relationships presented are discussed.

* Corresponding author.
E-mail address: jason.fox@nist.gov (J.C. Fox (3)).

https://doi.org/10.1016/j.cirp.2023.04.024
0007-8506/Published by Elsevier Ltd on behalf of CIRP.

2. Methods

2.1. Build design

The RTR sample was designed as a single-layer, irregular, convex octagon-shaped area, hereafter referred to as the tile, atop a rectangular prism. An example of the design is shown in Fig. 1. The samples were printed at the National Institute of Standards and Technology (NIST) on a commercially available EOS M290 system using vendor supplied IN625 powder. The tile contains a 5 mm × 5 mm square flanked by trapezoids that narrow to 1 mm at the left- and right-most sides. This was chosen to be on the order of single-track melt pool length measurements in prior work [19]. The bounding box of the tile was centered on the prism.

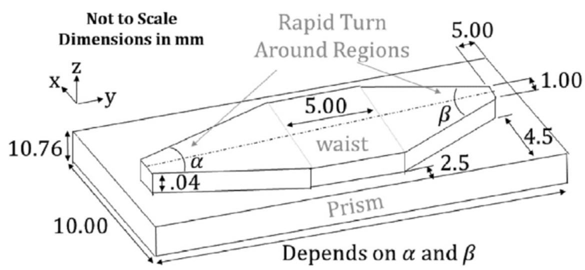

Fig. 1. Experiment sample design.

The angles α and β varied from 5° to 35° in combinations that minimized sample length in the x-direction. The length of the tile was also adjusted for each sample to maintain 5 mm of distance from the 10 mm edges of the prism. Thus, the value of α and β will change the length of the tile. The prism's height of 10.76 mm allowed the scan strategy to be defined with all laser tracks alternating travel direction between $\pm y$-directions, which is parallel to the 10 mm edges of the prism. This also allowed the sample to be printed as a single part, maintaining the 67° rotation from layer-to-layer. The melting of the tile therefore would start with the first track on the left-most or right-most end of the tile with tracks being added in the positive or negative x-direction, respectively. This step-over direction will be identified in figures and text as needed and the step-over distance is determined by the programmed hatch spacing. A full list of the process parameters used, including schematics of the scan path, are available in the supplemental material [20]. Two builds separated by approximately one year were performed. The specific samples investigated in this work, used the following settings: 1) Samples were built on 101.6 mm × 101.6 mm × 12.5 mm sub-plates, which are bolted to a modified full-size build plate (up to four sub-plates per build). 2) The upskin build strategy (i.e., different power/velocity settings near upward facing surfaces) was turned off to replicate behavior in bulk regions where subsequent layers are fused. 3) The laser power, laser scan speed, and hatch spacing were set to 295 W, 960 mm/s, and 110 µm, respectively. These three points are to mimic settings used in prior work [17,19].

For the two samples analyzed in this work, the first was fabricated in build 1 and used a 100 mm stripe width to minimize the effect of stripe boundaries. The effects of stripe boundaries have been shown to propagate height variations in 2+ layers above the boundary [19]. The second was fabricated in build 2 and stripe boundaries were removed entirely. The laser step-over direction, angle (i.e., α and β), and/or sample identifier are provided in the text and figures as needed for clarity. Sample identifiers are the following “B1-P3–15–20” and “B2-P2–15–15”. Format of the identifier is “B(Build #)-P(Sub-Plate #)-(α)-(β).”

2.2. Surface and melt pool boundary characterization methods

Topography measurements were performed using commercially available Zygo Zegage Pro-and NexView Coherence Scanning Interferometry (CSI) systems with Mirau objectives. Data was processed in the native software (20% stitching overlap) on the instrument (Mx ver. 8.0.0.26) and Mountains Map (ver. 9.0.9733).

To prepare the sample for melt pool boundary identification, the following steps were used. Wire electrical discharge machining (EDM) was used to bisect the sample on the dashed centerline in Fig. 1, then both halves of that part were removed approximately 1 mm above the sub-plate. The portion of the part closest to the back of the machine was mounted and metallographically prepared using an Aquia Regia etch to reveal the melt pool boundaries. After etching, micrographs were captured using a Zeiss AxioImager.Z2. Multiple micrographs were stitched together using ZenCore3.2 image acquisition and analysis software to image the entire tile region. Bright field micrographs taken at a total magnification of 200 × with a pixel size of 0.174 µm were used for melt pool measurements in ImageJ. Melt pool depth was determined by measuring the deepest point of a given melt pool to the surface directly above it. Melt pool trailing half-width was taken as the widest horizontal distance between the deepest point in the melt to the intersection point of the boundary and the top surface.

3. Results and discussion

3.1. Surface topography from build 1

Height data on B1-P3–15–20 is presented in Fig. 2. In Fig. 2a several phenomena can be seen: 1) Highly distorted melt pools are observed at the 15° and 20° angles (i.e., bottom and top of (a), respectively). 2) At the waist of the tile, there is a clear indication of double-wide melt pools at the edges and extending to the center of the waist. At the center of the waist, closer-to-nominal single-wide track geometries emerge, but the position at which these transitions occur is neither clear nor could a consistent pattern be found from initial analysis 3) There is a transition from the large, deformed melt pool in the center of the tile, to double-wide melt pools at the boundaries of the tile. Current efforts are attempting to identify quantitative methods for tracking the transitions.

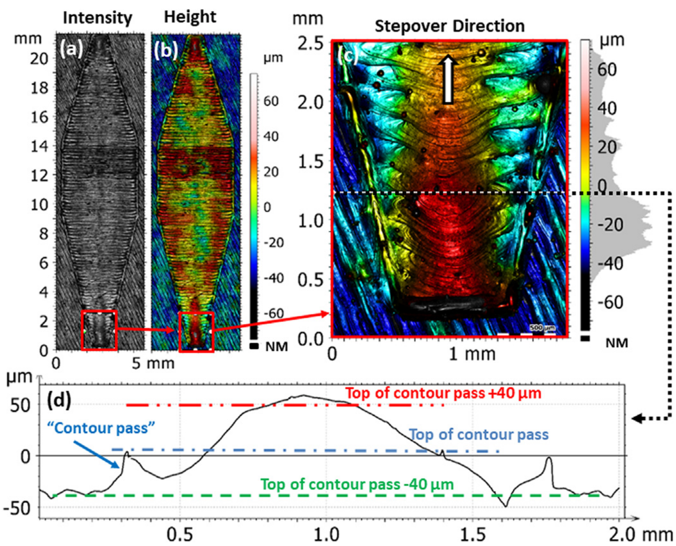

Fig. 2. Analysis of CSI data from sample B1-P3–15–20. a) Intensity and b) false color height map, both for the full tile. c) Enlarged view of the height map at the 15° end. d) Profile at the peak of the weld pool distortion. NexView 10x objective, 0.5x tube lens. High-resolution available online.

The extent of the deformation is further characterized in the enlarged images of the false color height and CSI intensity at the 15° end of the tile, presented in Fig. 2c, and a profile across the peak of the deformed melt pool is extracted and presented in Fig. 2d. Laser scan tracks in the part progress from the 15° end toward the 20° end. A profile measurement across the peak of the distorted melt pool shows that height deviations are greater than the 40 µm programmed layer thickness, similar to [19]. In the profile extracted from the height data, a blue dash-dot line shows the peak of the contour passes. The green dashed line, which is 40 µm below the top of the contour pass, aligns well with the previous layer seen on the left and right sides of the profile measurement. Additionally, the peak of the distortion at the 1 mm mark of the profile is <80 µm to the valley near the 0.5 mm mark on the left and <100 µm to the valley near the 1.7 mm mark on the right. Thus, within a single layer, the RTR is creating nearly three layers of height deviation, which is expected to have significant implications for part quality through potential recoater blade impacts and a greater potential for lack of fusion porosity.

3.2. Melt pool depth and trailing half-width comparison

The B1-P3–15–20 part was sectioned and prepared for melt pool boundary identification, as described in the Methodology section. Fig. 3 shows a top view of the sectioned part as well as the four regions where melt pool boundaries are identified. The part was further divided into two pieces prior to sample preparation. Site (I) is at the 15° end of the tile, site (IV) is at the 20° end, and sites (II)-(III) are at in the waist of the tile.

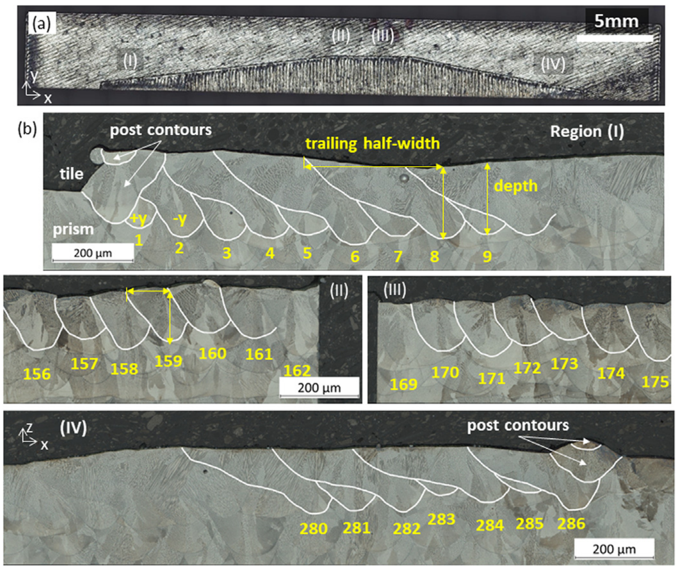

Fig. 3. (a) Top surface of sample B1-P3–15–20 with approximate location of sites (I) through (IV) identified and (b) corresponding side view, bright field optical micrographs. Some boundaries are traced for illustration purposes only. The stepover direction is to the right (track 1 to 286) with scan lines perpendicular to the step-over. Odd and even numbered tracks scan indicate the *+y* and -y directions, respectively. High resolution images available online [20].

The melt pool morphology in the waist, Fig. 3b (II) and (III), is typical. Some variation in depth and width but a uniform shape is observed. The melt pool morphology in the RTR regions is atypical with melt pools that have a large wing-like shape extending to the left and overlapping portions of several previous melt pools, Fig. 3b (I) and (IV). In between the large wing-like melt pools are tracks that cannot be traced back to the surface. This pattern of larger and smaller melt pools in the RTR regions is thought to be due to changing thermal conditions as the part is scanned. With the back-and-forth type of scan strategy, the melt pool will be at its largest near the start of a scan line and smallest near the end because the residual heat surrounding the melt pool has decreased over time. Therefore, some overlapping of larger and smaller melt pools is expected. While this wing-like melt pool shape has been seen in other work [14], the authors have not seen changes in size to the degree seen here.

Measurements of the melt pool depth and trailing half width are presented in Fig. 4. The RTR regions (I) and (IV) show marginally higher depths compared to the waist (II) and (III), particularly in (I).

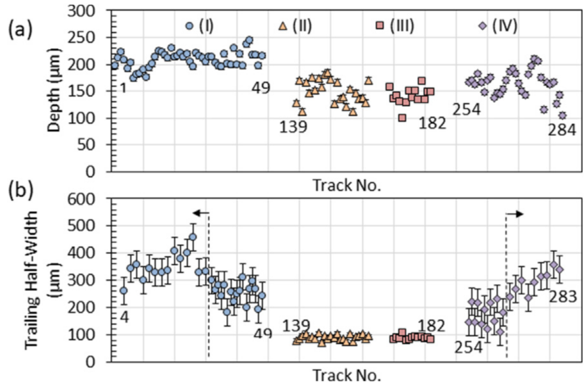

Fig. 4. Melt pool (a) depth and (b) trailing half-width at sites (I) through (IV). Track numbers are listed for the first and last measurement in each region. The x-axis grid represents 10 tracks. The vertical dashed lines on the width measurements are where a measurement is only possible for every other track. Error bars representing user selection uncertainty (k = 1) are ± 5 µm except for the region (I) and (IV) widths. The width measurements in these regions have a higher user uncertainty (± 50 µm). These conservative estimates are based on the pixel size and experience. Data for this figure is available online [20].

The difference in depth between (I) and (IV) is attributed to the change in the included angle of the tile and step-over direction (i.e., approaching or leaving an RTR). The trailing half-width shows significant differences between regions and a trend within the RTR regions. In region (IV), there is a clear increase in half-width due to the increase in residual heat as the melt pools approach the RTR tip. In position (I), there is an initial increase in the trailing half width, attributed to the build-up of residual heat in the first several lines of the tile, followed by a decrease in width. The decrease in width occurs as the length of the scan lines increases due to the 15° angle, resulting in a decrease in residual heat. The width is a minimum in the waist with no increasing or decreasing trend.

3.3. Surface topography from build 2 and conceptual model of RTR melt pool behavior

Fig. 5 shows an RTR from the 15° end of a tile from build 2. The step-over direction is to the left and, therefore, the final cooling of the melt pool in the tile can be seen at the left end of the tile. There is a large buildup of material in the center of the RTR with chevron patterns pointing to the right (i.e., like a greater than symbol >). At the last 500–600 µm of the tile, there is a region devoid of chevron patterns highlighted by the green arrow and dashed lines in Fig. 5. When manually segmented from the rest of the tile, the region devoid of chevron patterns was found to be quite smooth relative to the rest of the surface (Rq = 1.4 µm, Profile leveled, 2.5–250 µm double Gaussian bandpass filter). This is indicative of a single large melt pool rapidly freezing to leave a snapshot of the melt pool geometry at the laser spot, as seen in single track experiments by Fox et al. [15], and was similarly seen in both builds. Depressions located at the laser spot were also documented by Khairallah et al. [21]. The work also showed that the

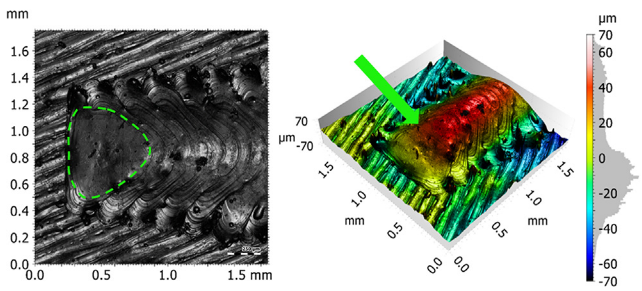

Fig. 5. The CSI intensity (left) and false color height with CSI overlay (right) for the RTR seen in the 15° end of part B2-P3–15–15. Laser scanning direction is vertical and step-over direction is to the left in the intensity (left) image. The green arrow and dashed line marks a region devoid of chevron patterns (20x mirau, 1x tube lens).

region behind the depression is dominated by surface tension (as opposed to the recoil force which dominates near the depression), which creates the buildup of material [21].

Using the 15° included angle to describe the physical phenomena, the track length decreases by 0.42 µm as the step-over moves toward the acute angle. As a result, the time it takes for each track to complete decreases as the tracks get closer to the narrow end of the acute angle. This decrease in time will result in an increase in residual heat as there is less time for the tracks to cool. Eventually, a transition where the residual heat is high enough to maintain an oversized melt pool moving in the step-over direction, rather than the single-wide melt pool moving in the laser scan direction, is expected. In Fig. 2a, this transition can be seen approximately 2 mm away from the 20° end.

Reversing the analysis for the start of the tile, the increase in time for the previous track to cool before the next track completes, which leads to a reduction in residual heat. However, the residual heat is also different for the starting vs. ending tracks of the tile. In the former, the first track is in powder with no residual heat from adjacent tracks. The second, third, etc. are influenced by the residual heat of the previous tracks. Based on this concept, we expect a transition point where the decrease in residual heat from the sequentially longer scan tracks is more influential then the residual heat from the previous tracks. This transition is seen around the 25th track of the trailing melt pool half-width measurements in Fig. 4, which also correlates well to the reduction in mound height around 2.5 mm to 3 mm from the 15° end of the tile (i.e., bottom of Fig. 2a). This is highly encouraging as the ideas presented can be generalized to predict melt pool distortions in fabrication of IN625 parts with vendor recommended parameters. To that end, future work will include expansion of the power/velocity combinations to better understaind how these methods can be applied outside of vendor recommended parametres. Furthermore, analysis of additional influencing factors to the residual heat will be performed (e.g., dwell time between layers, additional layers, other parts, etc.).

Finally, the importance of this result is magnified by the potential it implies. A strong understanding of the physical mechanisms that influence the resultant surface topography can create better correlations and predictions of surface topography. Thus, as researchers, we can lean on the extensive work investigating the process physics [21] and residual heat influencing the melt pool [18] to develop quantitative correlations.

4. Conclusion

IN625 samples built using a commercially available LPBF system were designed and analyzed to determine the relationship between the melt pool behavior and surface topography in RTRs. Measurements of surface topography, melt pool depth, and trailing half-width show deformations greater than 100 µm, which could create recoater blade impacts or increase possibility of lack of fusion porosity. Analysis of the melt pool depth and trailing half-width provided concrete evidence of oversized melt pools caused by the RTRs. These melt pools exhibited a wing-like shape, with very large trailing half-width that is attributed to the changes in residual heat. Evidence from the analysis was used to extend conceptual models to RTRs and correlations between the conceptual model and the surface topography show good agreement. Therefore, it is thought that a strong understanding of the thermal conditions at which the surface is formed can lead to quantitative correlations to the final surface topography.

Ongoing work is underway to replicate the study and assess the variation in these surface features under similar conditions. The processing window (e.g., laser power, scan speed, etc.) will be extended to quantify variation beyond the vendor recommended parameters. Future work will also include extension of the conceptual model into different materials and LPBF systems from other machine manufacturers to further quantify correlations between the process and surface topography.

Declaration of Competing Interest

The authors declare that they have no known competing financial interests or personal relationships that could have appeared to influence the work reported in this paper.

Acknowledgements and Disclaimer

This work was funded by the University of North Carolina at Charlotte's Center for Precision Metrology and the National Institute of Standards and Technology. NIST: J. Tarr (NIST) supported sample fabrication. UNCC: B. Mullany, A. Allen, and E. Morse supported conceptualization.

Certain commercial entities, equipment, or materials may be identified in this document to describe an experimental procedure or concept adequately. Such identification is not intended to imply recommendation or endorsement by the National Institute of Standards and Technology, nor is it intended to imply that the entities, materials, or equipment are necessarily the best available for the purpose.

References

[1] Zhang C, Wang S, Li J, Zhu Y, Peng T, Yang H (2020) Additive Manufacturing of Products with Functional Fluid Channels: A Review. *Additive Manufacturing* 36:101490.
[2] Chowdhury S, Yadaiah N, Prakash C, Ramakrishna S, Dixit S, Gupta LR, Buddhi D (2022) Laser Powder Bed Fusion: a State-of-the-Art Review of the Technology, Materials, Properties & Defects, and Numerical Modelling. *Journal of Material Research and Technology* 20:2109–2172.
[3] Everton SK, Hirsch M, Stravroulakis P, Leach RK, C lare AT (2023) Review of in-situ Process Monitoring and in-situ Metrology for Metal Additive Manufacturing. *Material & Design* .
[4] Grasso M, Colosimo BM (2017) Process Defects and in situ Monitoring Methods in Metal Powder Bed Fusion: a Review. *Measurement Science and Technology* 28:044005.
[5] Mandache C (2019) Overview of Non-Destructive Evaluation Techniques for Metal-Based AM. *Material Science and Technology* 35:1007–1015.
[6] 2018 America Makes & ANSI *Additive Manufacturing Standardization Collaborative Standardization Roadmap for Additive Manufacturing, Public Draft v2.0.*
[7] Whitehouse DJ (2010) *Handbook of Surface and Nanometrology*, .
[8] Jiang X, Scott PJ, Whitehouse DJ, Blunt L (2007) Paradigm Shifts in Surface Metrology. Part I. Historical philosophy. *Proceeding of the Royal Society A: Mathematical, Physical and Engineering Science* 463:2049–2070.
[9] Fox J, Allen A, Mullany B, Morse E, Isaacs R, Lata M, Sood A, Evans C (2021) Surface topography process signatures in nickel superalloy 625 additive manufacturing. In: *Proceedings of the Joint Special Interest Group Meeting Between euspen and ASPE*, . Advancing Precision in Additive Manufacturing.
[10] Levine L, Lane B, Heigel J, Migler K, Stoudt M, Phan T, Ricker R, Strantza M, Hill M, Zhang F, Seppala J, Garboczi E, Bain E, Cole D, Allen A, Fox J, and Campbell C (2020) Outcomes and Conclusions from the 2018 AM-Bench Measurements, Challenge Problems, Modeling Submissions, and Conference, *Integrating Material and Manufacturing Innovation* 9:1–15.
[11] Heigel JC, Lane BM, Levine LE (2020) In Situ Measurements of Melt-Pool Length and Cooling Rate During 3D Builds of the Metal AM-Bench Artifacts. *Integrating Material and Manufacturing Innovation* 9:31–53.
[12] Stoudt MR, Williams ME, Levine LE, Creuziger A, Young SA, Heigel JC, Lane BM, Phan TQ (2020) Location-Specific Microstructure Characterization Within IN625 Additive Manufacturing Benchmark Test Artifacts. *Integrating Material and Manufacturing Innovation* 9:54–69.
[13] Yadroitsev I, Gusarov A, Yadroitsava I, Smurov I (2010) Single track formation in selective laser melting of metal powders. *Journal of Material Research and Technology* 210:1624–1631.
[14] Yadroitsev I, Smurov I (2011) Surface Morphology in Selective Laser Melting of Metal Powders. *Physics Procedia* 12:264–270.
[15] Fox JC, Lane BM, Yeung H (2017) Measurement of Process Dynamics Through Coaxially Aligned High Speed Near-Infrared Imaging in LPBF AM. *Thermosense XXXIX* : 10214.
[16] Reese ZC, Fox JC, Taylor J, Evans C (2018) Evolution of Cooling Length in Parts Created Through Laser Powder Bed Fusion Additive Manufacturing. In: *Proceedings of the 2018 ASPE-euspen Topical Meeting*, Berkeley, CA183–188..
[17] Fox J, Sood A, Isaacs R, Brackman P, Mullany B, Morse E, Allen A, Santos E, Evans C (2022) Surface Feature Characteristics of LPBF of Nickel Superalloy 625 Bulk Regions. *Procedia CIRP* 108:531–536.
[18] Yeung H, Lane B (2020) A Residual Heat Compensation Based Scan Strategy for Powder Bed Fusion AM. *Manufacturing Letters* 25:56–59.
[19] Fox JC, Evans C, Sood A, Isaacs R, Mullany B, Allen AD, Morse E (2022) Weld Track Distortion In Laser Powder Bed Fusion Of Nickel Superalloy 625. In: *Proceedings of the ASPE-Euspen SIG Meeting*, . Advancing Precision in AM.
[20] Fox J, Evans C, Weaver J, Redford J, Surface Topography and Melt Pool Behavior in Rapid Turnaround Regions of Laser Powder Bed Fusion Additive Manufacturing of Nickel Superalloy 625, In: , NIST Public Data Repository.
[21] Khairallah SA, Anderson AT, Rubenchik A, King WE (2016) Laser Powder-Bed Fusion Additive Manufacturing: Physics of Complex Melt Flow and Formation Mechanisms of Pores, Spatter, and Denudation Zones. *Acta Material* 108:36–45.